Electronic Supplementary Material (ESI) for Journal of Materials Chemistry A.

Supporting Information

Tailoring the surface in copper manganese oxide materials and enhanced redox nature by graphitic carbon nitride sheets with ultra-long life for electrochemical applications

B. N. Vamsi Krishna and Jae Su Yu*

Department of Electronics and Information Convergence Engineering, Institute for Wearable Convergence Electronics, Kyung Hee University, Yongin-si, Gyeonggi-do 17104, Republic of Korea.

*Address correspondence to jsyu@khu.ac.kr

Session S1. Characterization

The crystalline phase of the prepared samples was investigated by X-ray diffraction (XRD, M18XHF-SRA, Mac Science). The structural properties of the synthesized samples were observed by using a field-emission scanning electron microscope (FE-SEM, LEO SUPRA 55, Carl Zeiss). The internal structural properties of the prepared samples were analyzed by using a transmission electron microscope (TEM, JEOL, JEM-2100F, 200 kV). To investigate the existed functional groups of the material, a Fourier-transform infrared spectrometer (FTIR, Thermo Nicolet – 5700) with a KBr pellet method was used. The X-ray photoelectron spectroscopy (XPS, Thermo Electron Multilab 2000) technique was used to analyze the surface composition of the prepared sample. The specific surface area properties of the sample were investigated by the Brunauer-Emmett-Teller (BET, BELSORP-max00131). The electrochemical measurements of the synthesized electrode materials were examined by an IVIUMSTAT workstation at normal room-temperature condition.

Session S2. Oxygen reduction reaction (ORR) measurements

The electrochemical catalytic properties of the prepared materials were determined by rotating ring disk electrode (RRDE), cyclic voltammetry (CV), rotating disk electrode (RDE), and linear sweep voltammetry (LSV) methods in oxygen saturated 0.1 M aqueous KOH electrolytic solution. Then, the three-electrode system was assembled by an active material coated glassy carbon electrode, Pt wire, and Ag/AgCl as the working, counter, and reference electrodes, respectively. For the preparation of working electrodes, the catalyst (CMO-90 or gCN-CMO) powder (50 wt%) and carbon black (50 wt%) were dissolved into the solution mixture of DI water (adequate amount) and Nafion ionomer (5 wt%, 0.35 mL) using ultrasonic stirring up to 20 min to acquire a

homogeneous slurry. Then, 0.36 μL of the prepared slurry was dispersed onto the glassy carbon electrode (diameter of 3 mm) by a micropipette, followed by drying over a lamp. For comparison, the commercially available Pt/C (20%) and IrO_2 electrodes were also prepared and evaluated under the same experimental conditions. The transferred electron number per O_2 molecule participated in ORR and the kinetic current density (J_k) was measured by the Koutecky-Levich (K-L) equation[1]:

$$J^{-1} = J_k^{-1} + (B\omega^{1/2})^{-1} \quad (1)$$

In the above equation, J_k is the kinetic current density and B is Levich slope, and B is given by the following equation[2]:

$$B = 0.62nFC_0(D_0)^{2/3}\upsilon^{-1/6} \quad (2)$$

where n is the transferred electron number, ω is the angular velocity of the disk in the oxygen molecule reduction, C_0 is the bulk concentration of oxygen (C_0= 1.2 × 10^{-6} mol cm^{-3}), D_0 is the diffusion coefficient of O_2 in 0.1 M aqueous KOH electrolyte, υ (υ = 0.01 cm^2 s^{-1}) is the kinematic viscosity of the electrolyte, and F is the Faraday constant (F = 96485 C mol^{-1}).

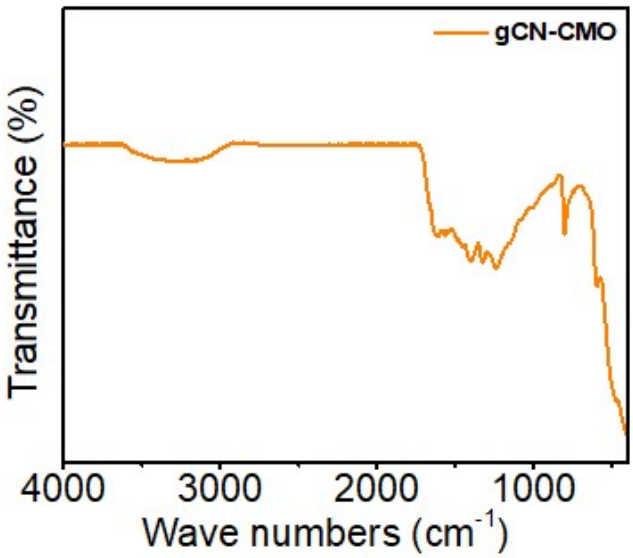

Figure S1. FTIR spectrum for the gCN-CMO material.

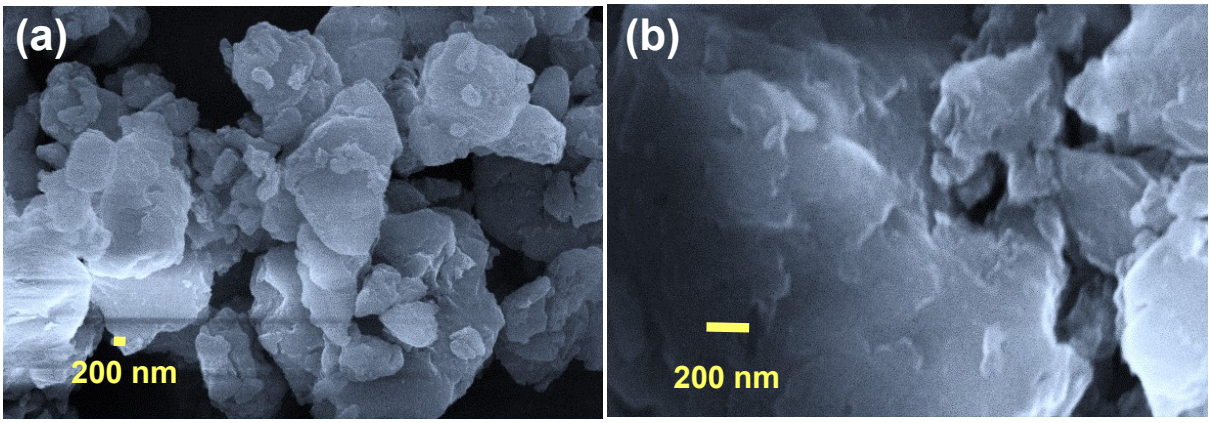

Figure S2. (a) Low- and (b) high-magnification FE-SEM images of the gC_3N_4 materials.

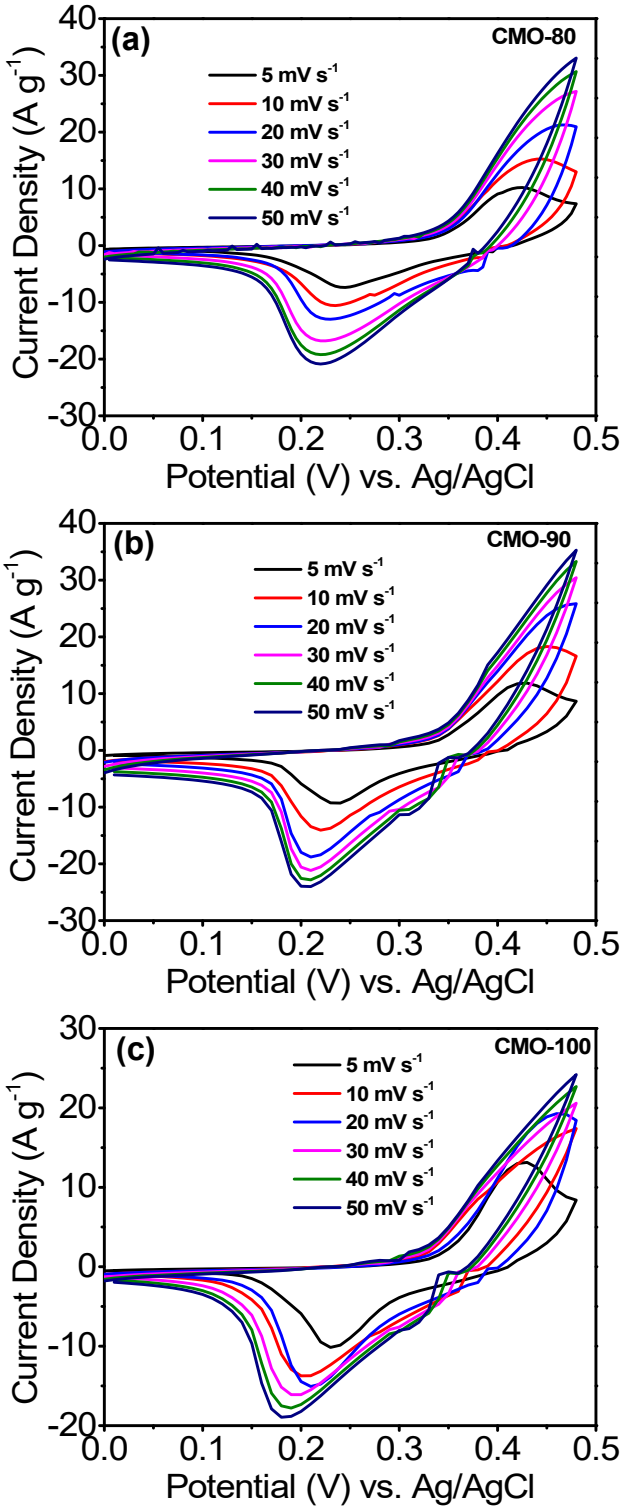

Figure S3. CV curves of the (a) CMO-80, (b) CMO-90, and (c) CMO-100 electrode materials at different scan rates.

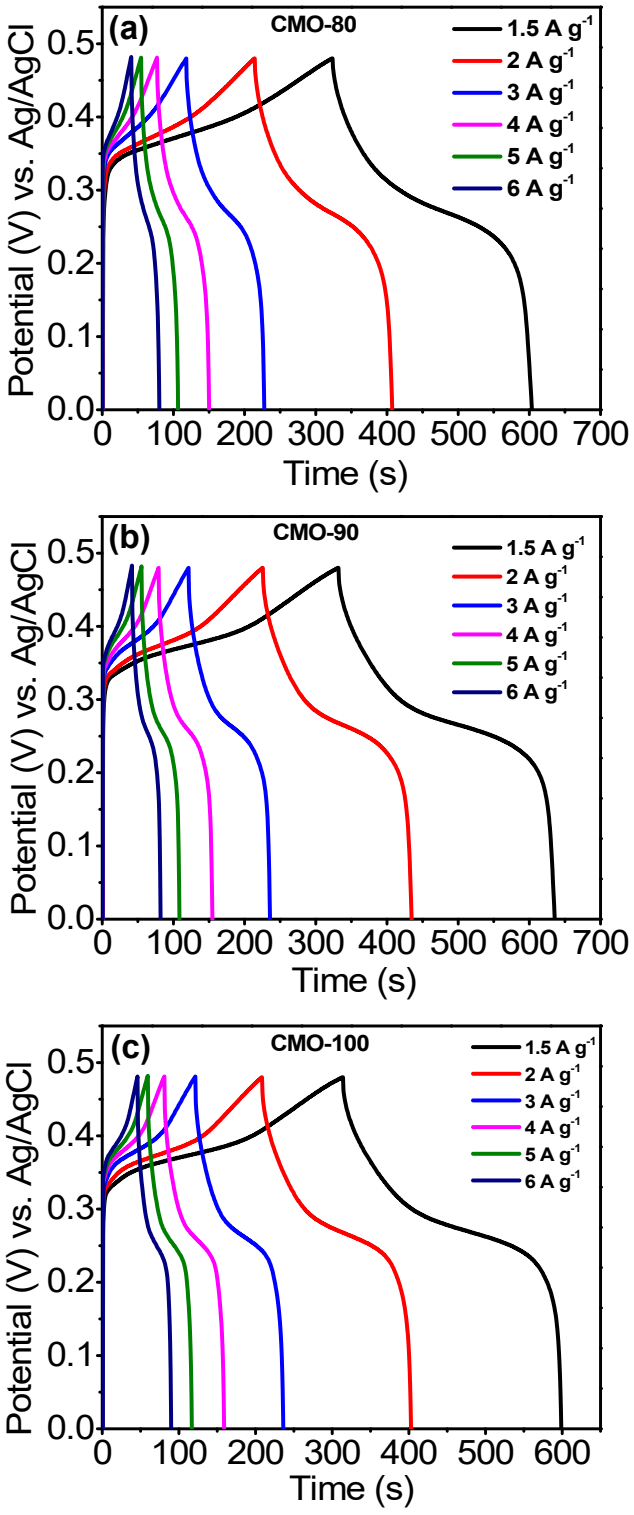

Figure S4. GCD curves of the (a) CMO-80, (b) CMO-90, and (c) CMO-100 electrode materials at various current densities.

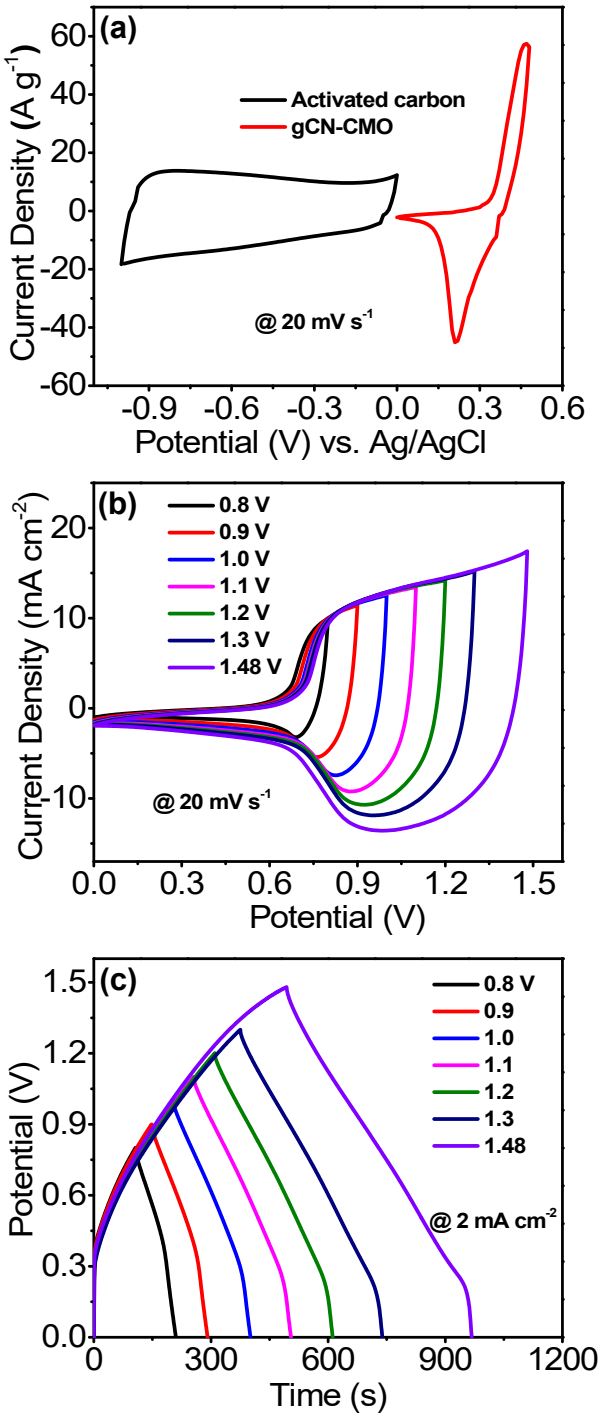

Figure S5. (a) CV curves of the AC and gCN-CMO electrode materials in 1 M KOH electrolyte at 20 mV s^{-1}. (b) CV curves at 20 mV s^{-1} and (c) GCD profiles at 2 mA cm^{-2} for the gCN-CMO//AC device at various potential windows.

Section S3. Electrochemical behavior of AC (anode) electrode

The CV profiles at various scan rates of 5, 10, 20, 30, 40, and 50 mV s^{-1} and the GCD profiles at different current densities of 1, 2, 3, 4, 5, and 6 A g^{-1} for the AC electrode were measured and displayed in Figure S6(a) and (b). The obtained CV curve shapes are in rectangular shapes with good reversibility at applied scan rates and there are no oxidation and reduction peaks, further suggesting the typical EDLC behavior of the AC electrode material. Figure S6(b) shows the corresponding measured GCD profiles of the anode electrode at various current densities. From Figure S6(b), the GCD curves revealed the typical EDLC nature ("V" shape or linear), which is well consistent with the obtained CV curve results of the AC electrode (Figure S6(a)). The specific capacitance (C_{ac}) for the AC electrode material was calculated by considering the discharge time profiles of the AC electrode at different current densities using the below well-known equation:

$$C_{ac} = \left(I \times \Delta t \right) / \left(m \times \Delta V \right) \quad (3)$$

In the above equation, I and Δt represent the current (A) and obtained discharge time (s), m represents the mass of the AC electrode coated on Ni foam which is 2 mg, and ΔV is the potential window of AC electrode. From the above equation, the estimated specific capacitance values of the AC electrode material were 230, 188, 171, 152, 140, and 132 F g^{-1} at the current densities of 1, 2, 3, 4, 5, and 6 A g^{-1}, respectively, as depicted in Figure S6(c). Additionally, the FE-SEM image of the AC electrode material is shown in Figure S6(d), in which AC material was mixed with PVDF binder coated on Ni foam and the corresponding magnified image is shown in the inset of Figure S6(d).

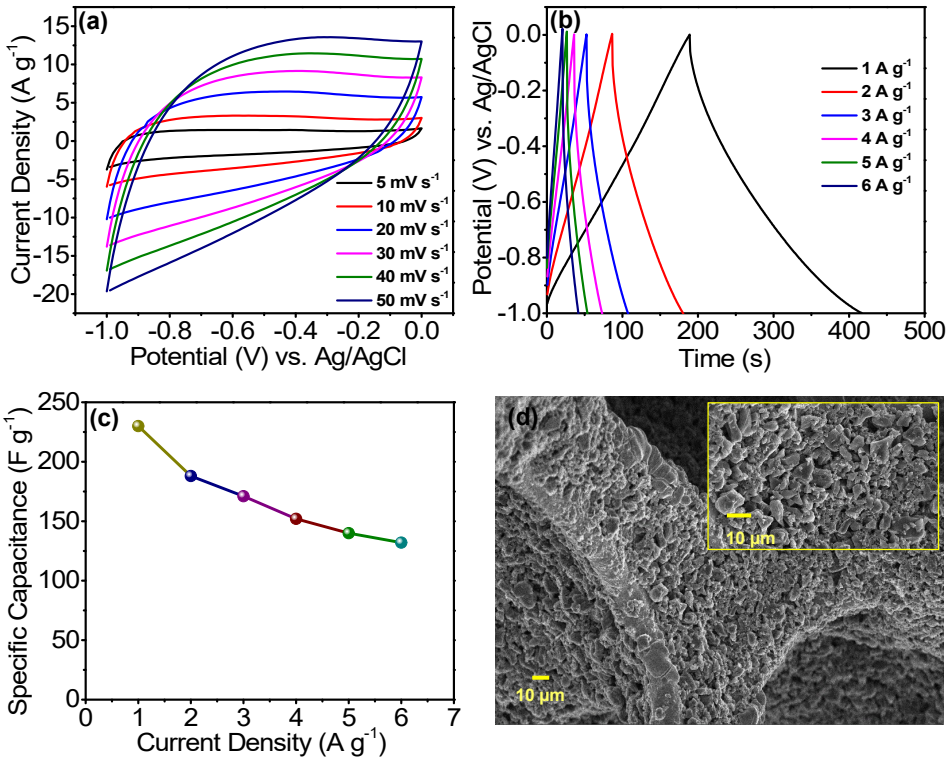

Figure S6. (a) CV curves (5 to 50 mV s^{-1}), (b) GCD curves (1-6 A g^{-1}), and (c) specific capacitance values of the AC electrode at various applied current densities. (d) FE-SEM image of the AC electrode.

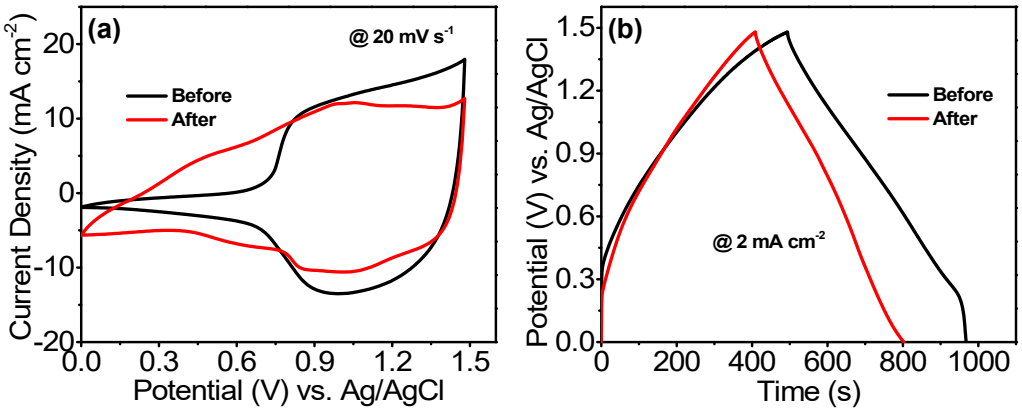

Figure S7. (a) CV curves at a scan rate of 20 mV s^{-1} and (b) GCD curves at a current density of 2 mA cm^{-2} for the gCN-CMO//AC device before and after 100000 cycles.

Session S4. Electrocatalytic properties

Figure S8(a) and (b) shows the LSV curves on the RDE for the CMO-90 and gCN-CMO materials with a scan rate of 5 mV s^{-1} at various rotation speeds of 500, 1000, 1500, 2000, and 2500 rpm. The polarization plots reveal that the limiting current density values for the two samples (CMO-90 and gCN-CMO) increased with the disk rotation speed, which can be demonstrated by the rapid diffusion of ions at high rotation speeds. Moreover, the RDE curves for iridium oxide (IrO_2), CMO-90, gCN-CMO, and Pt/C samples at a constant rotation speed of 2500 rpm are represented in Figure S8(c). The current density of the gCN-CMO sample (4.44 mA cm^{-2}) was relatively higher than the IrO_2 (2.03 mA cm^{-2}) and CMO-90 (3.78 mA cm^{-2}) samples (Figure S8(c)), indicating the good electrocatalytic property of the gCN-CMO material towards ORR. However, the electrocatalytic performance of all the prepared materials is still low compared to the Pt/C material (5.30 mA cm^{-2}) (Figure S8(c)). Figure S8(d) shows the K-L plots of the CMO-90, gCN-CMO, and Pt/C materials at a fixed potential of 0.4 V versus reversible hydrogen electrode (RHE). In addition, the number of electrons associated with the ORR process is a crucial parameter to estimate the electrocatalytic ORR in the electrolyte solution[3]. The electron transfer numbers for the CMO-90, gCN-CMO, and Pt/C samples were measured and compared with the theoretical values (n= 2 or 4) as shown in Figure S8(d). The K-L plots revealed almost constant slope and excellent linearity over the potential for the gCN-CMO sample (Figure S8(d)), signifying that during the ORR treatment, the electron transfer values are very stable at various potentials. Mainly, the electron transfer number per O_2 molecule during the kinetic current density (J_k) and ORR were evaluated from the K-L equation. The n values measured from the K-L plot at a specific potential of 0.4 V

vs. RHE for CMO-90, gCN-CMO, and Pt/C materials were estimated to be 3.7, 3.9, and 4.0, respectively. This implies that the gCN-CMO material reveals a much better n value than the CMO-90 material. The average n value of the gCN-CMO sample was estimated to be 3.9, representing nearly 4 electron transfer process for ORR. These results suggest that the ORR catalytic performance could be enhanced greatly when the conductive and porous gC_3N_4 sheets were introduced into the sample. The obtained electrocatalytic results are in good agreement with the electrochemical properties of the prepared materials. The commendable ORR properties of the gCN-CMO material could be a promising ORR electrocatalyst material.

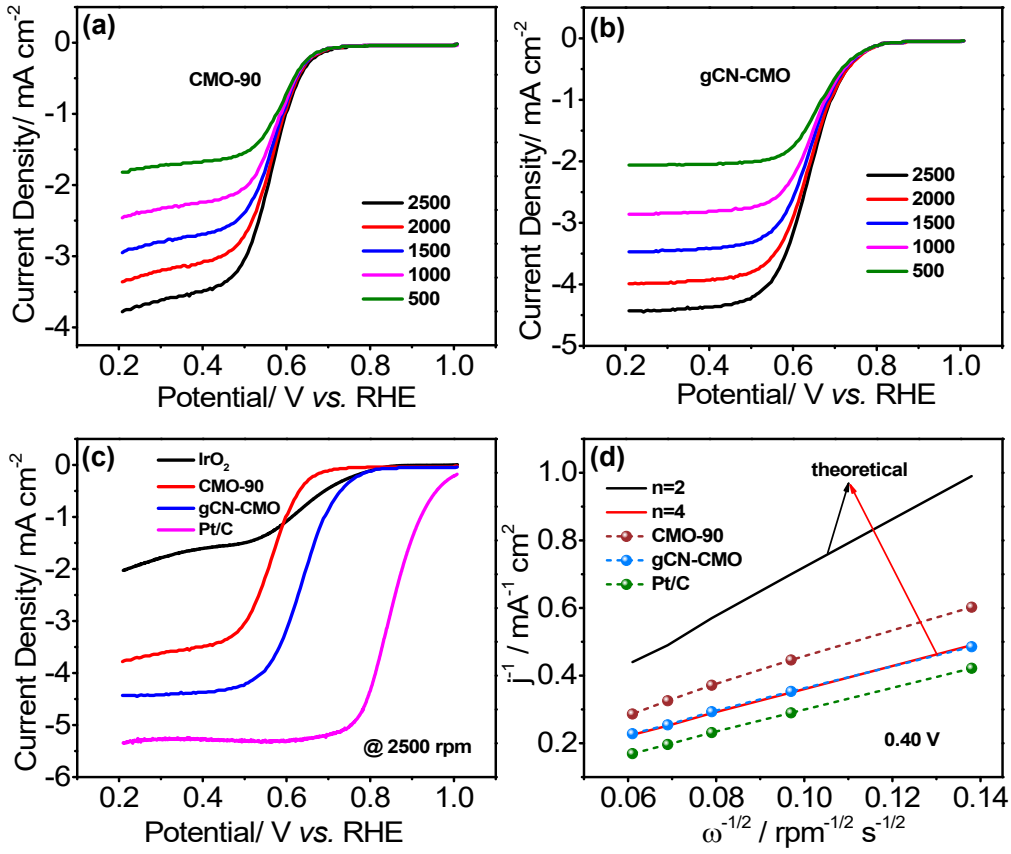

Figure S8. Linear sweep voltammograms of the (a) CMO-90 and (b) gCN-CMO materials at a scan rate of 5 mV s^{-1}. (c) Oxygen reduction polarization curves of the CMO-90, gCN-CMO, Pt/C,

and IrO_2 catalysts at a constant rotation speed of 2500 rpm. (d) K-L plots at 0.4 V vs. RHE for the CMO-90, gCN-CMO, and Pt/C.

Session S5. Charge storage mechanism

The observed CV curves (Figure 4(e)) which purely exhibited that the oxidation and reduction of metal ions present in the gCN-CMO material may be due to the Cu^{1+}/Cu^{2+} or Mn^{3+}. Furthermore, the intercalation/deintercalation of K^+ ions into the tunnels of material is also supporting the charge storage process. The possible redox reactions in the time of electrochemical study for the gCN-CMO electrode are as follows[4, 5]:

$$CuO + H_2O + 2\,e^- \leftrightarrow Cu_2O + 2OH^- \quad (4)$$

$$MnO_2 + H^+ + e^- \leftrightarrow MnOOH \quad (5)$$

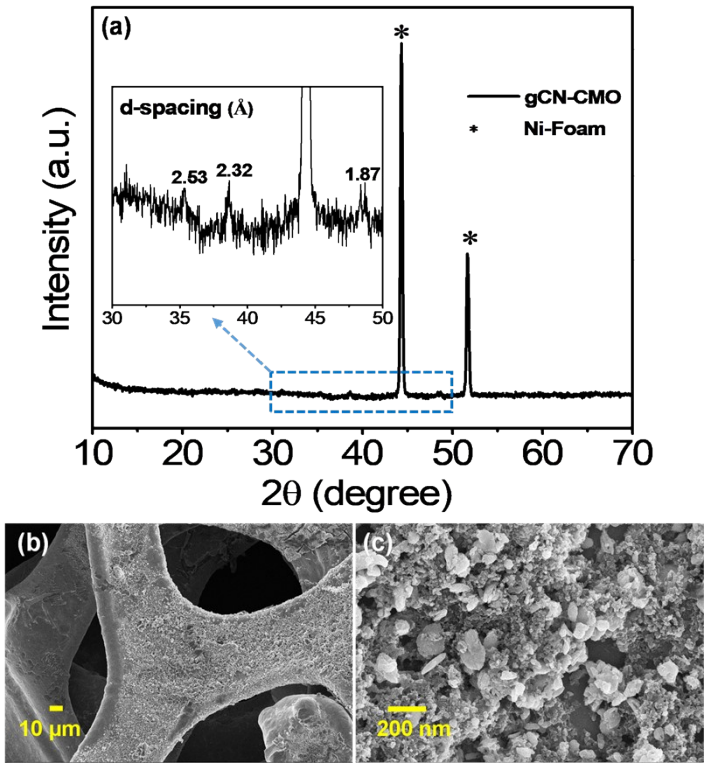

Figure S9. (a) the XRD pattern and (b,c) low- and high-magnification FE-SEM images of the gCN-CMO electrode measured after the long cycling test in a two-electrode system.

Table S1. Electrochemical performance comparison of the prepared gCN-CMO electrode material with the previously published metal copper and manganese-based electrode materials.

Composite material	Synthesis method	Electrolyte	Performance	Cycling stability@ Retention	Reference
β-MnO_2 NBs	Hydrothermal method	6 M KOH	362 F g^{-1} @ 1 A g^{-1}	10000 cycles @ 2 A g^{-1} @ 96.3%	6
Cu_2O microcubes	Hydrothermal method	6 M KOH	660 F g^{-1} @ 1 A g^{-1}	1000 cycles @ 5 A g^{-1} @ 80%	7
Co_3O_4/g-C_3N_4	Precipitation method	6 M KOH	1071 F g^{-1} @ 1 A g^{-1}	4000 cycles @ 10 A g^{-1} @ 80%	8

Co_3O_4@g-C_3N_4	One-pot mechanochemical green synthetic	-	457.2 F g^{-1} @ 1 A g^{-1}	5000 cycles @ 10 A g^{-1} @ 92%	[9]
$CuCoO_2$	Hydrothermal method	-	250 F g^{-1} @ 0.5 A g^{-1}	5000 cycles @ 5 A g^{-1} @ 81.36%	[10]
$CuNiO_2$	One-step hydrothermal	3 M KOH	153.02 mAh g^{-1}@ 2 A g^{-1}	3000 cycles @ 6 A g^{-1} @ 94.14%	[11]
$CoMnO_2$@PICF-6	Hydrothermal method	1 M KOH	928 F g^{-1} @ 1 A g^{-1}	3000 cycles @ 2.8 A g^{-1} @ 95%	[12]
CuO@MnO_2	Hydrothermal method	-	343.9 F g^{-1} @ 0.25 A g^{-1}	12000 cycles @ 5 A g^{-1} @ 83.1%	[13]
$CuMnO_2$/GQD	Hydrothermal method	3 M KOH	520.2 C g^{-1} @ 1 A g^{-1}	5000 cycles @ 7 A g^{-1} @ 83.3%	[14]
$CuMn_2O_4$-RGO	Sol-gel method	1 M Na_2SO_4	342 F g^{-1} @ 1 A g^{-1}	10000 cycles @ 5 A g^{-1} @ 75.5%	[15]
$CuMnO_2$ nanoparticles	Hydrothermal method	PVA-KOH gel electrolyte	765 F g^{-1} @ 5 A g^{-1}	18000 cycles @ 1 A g^{-1} @ 80%	[16]
$CuCo_2O_4$	Hydrothermal method	PVA/KOH gel	1006 F g^{-1} @ 1 A g^{-1}	10000 cycles @10 A g^{-1} @ 71.2%	[17]
gCN-CMO	A facile silicon oil bath method	1 M KOH	250 mAh g^{-1} (1844 F g^{-1}) @ 1.5 A g^{-1}	100000 cycles @ 20 mA cm^{-2} @ 84%	Present work

References

1. D. Yu, Y. Xue and L. Dai, *J. Phys. Chem. Lett.*, 2012, **3**, 2863-2870.

2. J. Li, Y. Ren, S. Wang, Z. Ren and J. Yu, *Appl. Mater. Today*, 2016, **3**, 63-72.

3. S. Sarkar, S. S. Sumukh, K. Roy, N. Kamboj, T. Purkait, M. Das and R. S. Dey, *J. Colloid Interface Sci.*, 2020, **558**, 182-189.

4. A. K. Mishra, A. K. Nayak, A. K. Das and D. Pradhan, *J. Phys. Chem. C*, 2018, **122**, 11249-11261.

5. C. Wu, Y. Zhu, M. Ding, C. Jia and K. Zhang, *Electrochim. Acta* 2018, **291**, 249-255.

6. S. Zhu, H. Zhang, P. Chen, L. H. Nie, C. H. Li and S. K. Li, *J. Mater. Chem. A*, 2015, **3**, 1540-1548.

7. R. Kumar, P. Rai and A. Sharma, *RSC Adv.*, 2016, **6**, 3815-3822.

8. Y. Zhang, L. Chang, X. Chang, H. Chen, Y. Li, Y. Fan, J. Wang, D. Cui and C. Xue, *Diam. Relat. Mater.*, 2021, **111**, 108165.

9. I. Rabani, R. Zafar, K. Subalakshmi, H. S. Kim, C. Bathula and Y. S. Seo, *J. Hazard. Mater.*, 2021, **407**, 124360.

10. M. Isacfranklin, R. Yuvakkumar, G. Ravi, M. Pannipara, A. G. Al-Sehemi and DhayalanVelauthapillai, *Mater. Lett.*, 2021, **296**, 129930.

11. C. S. Song, C. V. V. M. Gopi, R. Vinodh, S. Sambasivam, R. M. N. Kalla, I. M. Obaidat and H. J. Kim, *J. Energy Storage*, 2019, **26**, 101037.

12. Y. H. Cho, J. G. Seong, J. H. Noh, D. Y. Kim, Y. S. Chung, T. H. Ko and B. S. Kim, *Molecules*, 2020, **25**, 5863.

13. H. Chen, M. Zhou, T. Wang, F. Li and Y. X. Zhang, *J. Mater. Chem. A*, 2016, **4**, 10786-10793.

14. M. Ashourdan, A. Semnani, F. Hasanpour and S. E. Moosavifard, *Journal of Energy Storage*, 2021, **36**, 102449.

15. C. Zhang, A. Xie, W. Zhang, J. Chang, C. Liu, L. Gu, X. Duo, F. Pan and S. Luo, *J. Energy Storage*, 2021, **34**, 102181.

16. L. Wang, M. Arif, G. Duan, S. Chen and X. Liu, *J. Power Sources*, 2017, **355**, 53-61.

17. Y. Feng, W. Liu, Y. Wang, W. Gao, J. Li, K. Liu, X. Wang and J. Jiang, *J. Power Sources*, 2020, **458**, 228005.